Nanosilica to improve the flowability of fine limestone powders in thermochemical storage units

R. Gannoun [a], J.M.P. Ebrí [a], A.T. Pérez [a], M.J. Espín [b], F.J. Durán-Olivencia [a], J.M. Valverde [a],*

[a] *Facultad de Física, Universidad de Sevilla, Avda. Reina Mercedes s/n, 41012 Seville, Spain*
[b] *Dpto. de Física Aplicada II, Universidad de Sevilla, Avda. Reina Mercedes s/n, 41012 Seville, Spain*

ARTICLE INFO

ABSTRACT

Fine powders are the cornerstone of new energy storage solutions to assist concentrated solar power plants. Though, their ability to behave like fluid can be seriously affected at high temperatures. This work investigates the use of nanosilica in fine limestone (calcium carbonate, $CaCO_3$) powders to mitigate the promotion of cohesion forces at high temperatures. Experiments were conducted over limestone powder samples with particle sizes around $45\,\mu m$. The analysis was performed monitoring the tensile yield strength as the samples were subjected to different temperatures and consolidation stresses while varying the nanosilica content up until 0.82 wt%. Temperatures reached a maximum of 500 °C (close to the Tamman temperature in limestone), whereas consolidation stresses were increased up to 2 kPa. Results show that nanosilica coating is an efficient solution to inhibit the enhancement of powder cohesiveness at high temperatures and consolidations. A solution that offers better control to smooth the granular flow regimes in production environments.

1. Introduction

Limestone powders, nearly 100% calcium carbonate ($CaCO_3$), are used to operate new thermochemical energy storage technology [1]. A solution devised to assist concentrated-solar-power (CSP) plants channeling the solar energy from the receiver to the storage unit [2–4]. It is in these two extremes of the storage circuit where granular-based solutions surpass the performance of their molten salt counterparts [5]. However, liquid-based solutions are unbeatable when it comes to transport the material from end to end. Certainly, granular flows may exhibit jamming and other issues that eventually may lead to intermittent flow regimes. This is especially relevant in fine powders, which would be the best candidates in gas–solid reactive flows that require large contact areas, if not for such issues.

Fine powders are usually cohesive, and their cohesiveness is often enhanced significantly at high temperatures [6]. This is one of the most controversial features of new granular-based storage designs. Unlike coarser granular media like sand, in fine powders delimiting the turning point from which adhesion forces govern the powder flowability is a challenge. In contrast to coarser granular materials, in fine powders adhesion forces can be much higher than their weight at ambient temperature [7]. Surface deformation at particles contact, interparticle diffusion, reactivity between grains, or atomic/ion mobility at surface level are some factors that may well unbalance the adhesion/weight

relationship favoring the clustering among grains. Thus, fine powders are much more prone to suffer significant variation in their flowability as all these factors intertwined as temperature raises [6,8,9]. Indeed, characterizing and controlling the flowability in fine powders is still one of the most critical issues in many industries, such as flour [10,11] or cement industries [12]. Therefore, a better understanding of the granular flow regimes is of paramount importance within the European research project (H2020) developed by the authors [13]. The main goal of this project is to prove the feasibility of thermochemical energy storage solutions to assist CSP plants via fine limestone powders.

The first CSP pilot plant assisted by thermochemical storage units in the EU (currently under construction [13]) implements the calcium looping (CaL) process devised by Shimizu et al. [14]. The CaL cycle [15–17] is governed by a reversible solid–gas reaction [18]. The endothermic part of this reaction —the calcination process— absorbs the solar radiation collected at the receiver. As a result, the heat is stored in the form of chemical potential. Later the exothermic reaction —the carbonation process— unleashes all this heat during the discharge phase at the generator. The heat released in this sector maps the high temperatures reached at the receiver. As it turns out, higher temperatures lead to more efficient thermodynamic cycles. Certainly, heat transfer or chemical reactivity are central factors to keep the overall performance [19]. But, the transport of the granular material

from both ends is by far the most critical aspect of this technology. Production environments demand uninterrupted granular flows, which, in turn, requires more precise control of powder flowability.

Particle size is very essential in this matter [9,20]. It modulates (1) the amount of material exposes to react and (2) the relation between surface and volume forces shaping the intensity of cohesion forces. Thus, the smaller the particle size, the more important the attractive forces (cohesion) between particles become compared to their weight. As a result, as the particle size decreases, the granular flow regime shifts from the free-flowing area to the cohesive region, where the airflow drag is no longer enough to fall apart the aggregates.

At the working conditions in thermochemical storage units in CSP plants, the pore plugging effect severely limits the carbonation reaction for particle size above 50 μm, approximately [19,21–25]. At ambient temperature, 50 μm particle size delimits a fuzzy boundary depending on the material [7] that serves to differentiate between free-flowing and cohesive behaviors.

Fluidization promoted by fine particles not only favors the transport but also enhances the kinetics in entrained flow reactors. A reactor design [13,17,18,26,27] that has proven to be the optimal architecture for the calcination process at the receiver in CSP facilities. Though, these reactors involve short solid residence time—the reason why, they require fine powders to boost the chemical activity [28,29]. The downside of fine powders within the context of thermochemical storage units is that their flowability is more vulnerable to the impact of temperature [20,30,31]. In fact, around the 50 μm particle size boundary at ambient temperature, van der Waals attraction forces between particles balance their weight [20]. The increase in temperature quickly unbalances this situation; temperature favors particle mobility and reactivity, which eventually leads to larger powder cohesiveness.

As it has been reported, fine limestone powders are critically affected by temperature [6,8,9]. Limestone flowability decreases significantly as the temperature approaches the Tamman temperature (545 °C [32,33]); the temperature at which atoms or ions mobility in solids becomes appreciable, favoring thus the sintering process. Recent studies with fine limestone powders measured an increment up to one order of magnitude in the tensile yield strength at 500 °C [6,8]. The authors used particles size around 45 μm, applying a consolidation stress of 2 kPa before fluidizing the sample and monitoring its tensile yield strength. Authors showed that the consolidation stress enhances the cohesion forces significantly, worsening thus the effect of temperature on the limestone flowability. These results align with the softening that occurs at the contact between solids at high temperatures [20]. With a larger contact area, adhesion forces increase, and powder flowability declines accordingly.

Nanosilica has shown to be an additive able to reduce the power cohesiveness at ambient temperature [34–38]. These results apply if nanosilica eventually coat powder particles after the mixing process. The coating acts as an armor layer that increases the mechanical hardness of the modified powder particle [39–41]. Furthermore, as particles are less prone to deform at the contact, the effective interaction area is reduced considerably. Thus, shielding powder particles with nanosilica tend to deplete attractive forces at the contact. Recent experimental studies confirmed the effectiveness of the nanosilica coatings in limestone at ambient temperature [42]. More importantly, the shielding effect has also been reported to be effective in limestone at high temperatures [6].

Within this context, this work aims at investigating the optimal amount of nanosilica coating to mitigate flowability issues in CSP facilities assisted with thermochemical storage units.

To that end, this work analyzes the evolution of cohesion forces in limestone as the amount of nanosilica increases gradually up to 0.82 wt%. Experiments monitored the tensile yield strength of the limestone powder as the temperature increased up to 500 °C (close to the Tamman temperature in limestone). To clarify the nanosilica shielding effect (increasing the hardness of the material), powder samples were consolidated up to 2 kPa before monitoring the tensile yield strength through the fluidization regime. The results confirm that nanosilica is an excellent candidate to ease the limestone cohesiveness at high temperatures. For instance, in the worst scenario analyzed in this work (at 500 °C with powder sample subjected to a previous consolidation stress of 2 kPa), the tensile yield strength was reduced by roughly 50%. Thus, modified particles behave as if they operated 200 °C below the actual temperature (500 °C). An outcome that might be critical to alleviate flowability issues when limestone powders must operate near the Tamman temperature while transporting the granular material from the calciner to the storage unit.

This work has been carried out within the framework of the H2020 European project SOCRATCES [13] coordinated by the University of Seville, whose goal is to demonstrate at the pilot scale the suitability of the Calcium Looping process to store energy using fine limestone powders.

2. Materials and experimental setup

In what follows, the materials and the experimental setup used in this work are introduced in detail.

2.1. Materials

Experiments were performed on fine limestone powders (99.1% $CaCO_3$), supplied by KSL Staubtechnik Gmbh (Eskal45). The average particle size was about $d_p = 41.5$ μm. More importantly, particle size exhibited a very sharp distribution around the average [8], which is essential to control potential size effects throughout the experiments.

Two types of powder samples were used in the experiments: (1) the raw samples and (2) samples coated with fumed nanosilica (Aerosil R974 from Evonik) at different wt%. The coating process was undertaken via simple dry-mixing in a rotating drum [36,43]. This method layers limestone particles uniformly with nanosilica aggregates, whose size is around 100 nm (Fig. 1,2) [44].

Table 1 outlines the mechanical properties of the materials studied in this work. According to the literature, there exists no clear consensus about the values of these mechanical properties. Data vary broadly among different studies, partly because of the use of different procedures and settings.

2.2. Experimental setup

The experimental setup used in this work is based on the Sevilla Powder Tester (SPT), which was originally proposed by Valverde et al. [62]. During the last years, the SPT design has been extensively used in powder characterization studies [44,63–68]. This work used an upgraded version of the SPT setup to measure the tensile yield strength at high temperatures [6,8] (Fig. 3).

The test cell consisted of a vertical cylindrical quartz tube of 4.5 cm diameter. Wall effects are negligible [39] as the height of the powder bed (about 2.8 cm) is always kept below the diameter of the cell. At the bottom of the cell, a porous ceramic plate was used to distribute the airflow across the bed uniformly. Before pumping the airflow through the bed, it was filtered and dried. The cleaning sequence eliminates both potential pollutants and moisture, which could have an impact on powder cohesiveness. This was achieved by a set of filters and an air dryer (model SMC IDFA3E). Dried and purified, the air stream was passed across the bed using a mass flow controller (Omega model FMA-2606 A, 2000 sccm). A set of electric valves enable a bidirectional flow through the bed. Upward, for breaking the powder bed through a fluidization cycle. And, downward, to impose a given consolidation stress on the sample. In both cases, the pressure drop across the bed was measured by a differential pressure transducer (MKS model 220CD, 10 Torr full scale). A sound generation system was used to produce a low-frequency sound wave driven by a PVC pipe to the top of
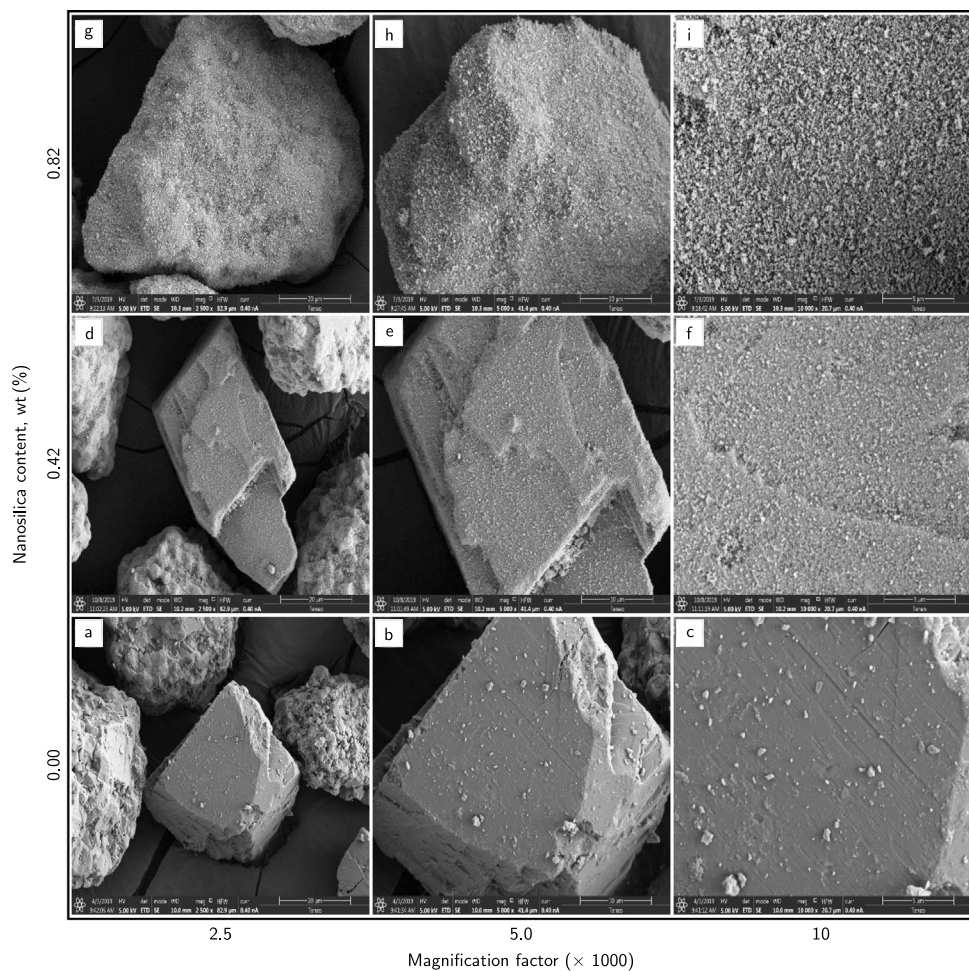
Fig. 1. Scanning electron microscopy (SEM) images of the limestone particles used in this work mixed with silica at different weight ratios: (a-c) 0 wt%; (d-f) 0.42 wt%; (g-i) 0.82 wt%.
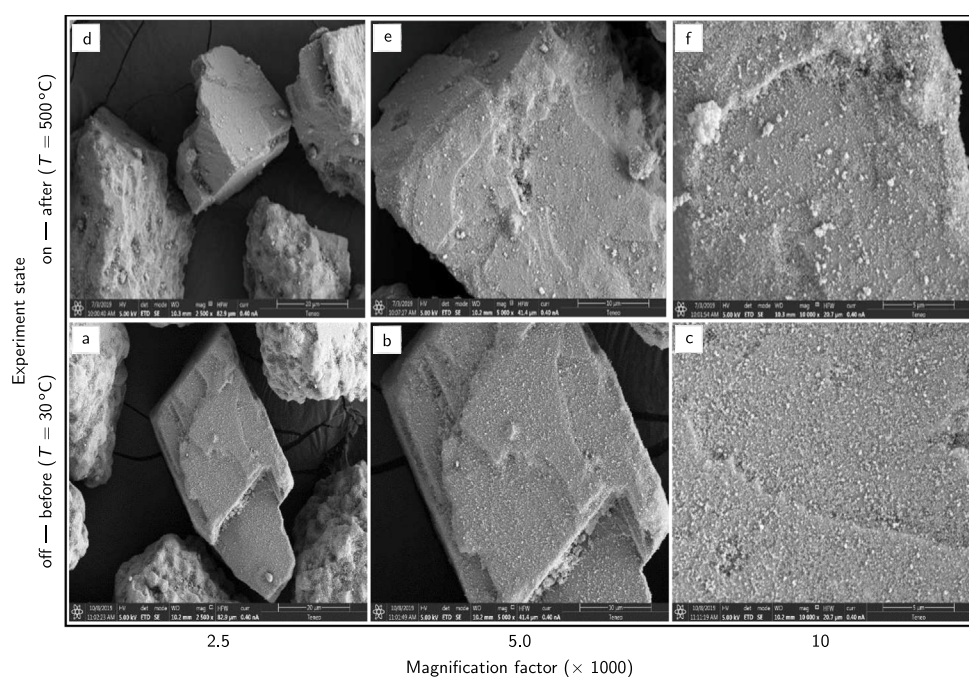

Fig. 2. Scanning electron microscopy (SEM) images of limestone particles coated with nanosilica (0.42 wt%): (a-c) sample at 30 °C before the tests, and (d-f) after the tests carried out at 500 °C.

Table 1

Material properties at room temperature reported in the literature for the powders tested in this work.

Materials	Density ρ_p (kg/m^3)	Diameter d_p (μm)	Young's modulus H (GPa)	Mechanical hardness E (GPa)	Poisson ratio γ (J/m^2)	Surface energy v (-)
CaCO$_3$	2700[a]	41.52[a]	(25, 88.19)[b]	(0.75,5.11)[c]	(0.21, 0.34)[d]	(0.32, 0.347)[e]
SiO$_2$ (fumed silica)	2200[a]	≈0.1[a]	74[f]	6[f]	0.17[g]	0.025[h]

[a]Data provided by the supplier.
[b][45–52].
[c][46,49,50,53,54].
[d][45–48,55–58].
[e][58,59].
[f][44].
[g][60].
[h][61].
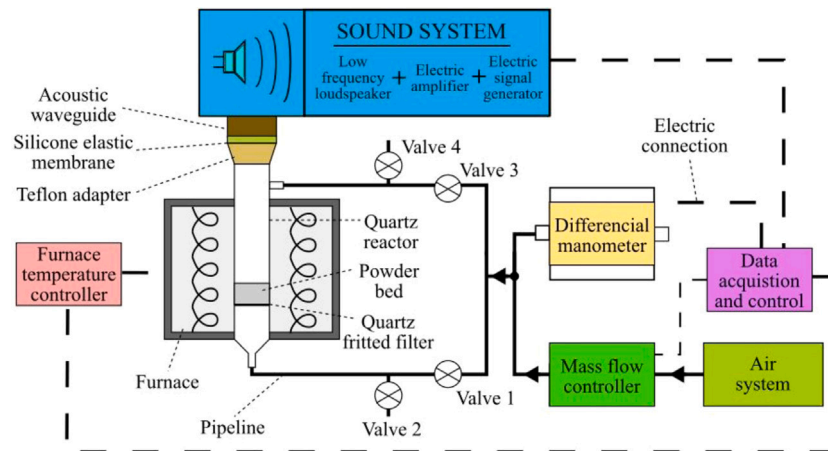
Fig. 3. Schematic representation of the experimental setup. More details about the method, procedure, and protocol can be found in Refs. [6,8,62].

the bed. This pipe was endowed with a silicone membrane to avoid contamination by elutriated particles in the sound generation system and keep the cell sealed.

The whole measuring process was controlled and automated using a protocol devised in LabView [6,8]. Before performing any test, the effect of the porous ceramic plate used for gas distribution was calibrated measuring the pressure drop in the absence of material. This pressure drop must be subtracted from the total one when the measure was performed with the powder sample, Δp. To initialize the powder in a reproducible state, the bed was fluidized by imposing a gas velocity much higher than the minimum fluidization velocity. The resulting bubbling regime was held for 30 s. During the first 5 s of this initialization period, an acoustical excitation of 150 dB at 130 Hz was applied to aid the fluidization of strongly cohesive samples. Then the gas flow was stopped, and the bed let to settle for 30 s.

To heat the samples up to the target temperature, the testing cell was placed inside an electric furnace controlled by a PID temperature controller (Eurotherm 3126). A thermal stabilization time of 1 h was set after reaching the desired temperature (ranging between ambient and 500 °C). Afterward, the sample was consolidated by a downward-directed gas flow to a target consolidation stress that varied between the powder weight per unit area (in the absence of consolidating air flow) and 2 kPa. The consolidating gas flow was kept fixed for 10 s. When the target consolidation stress was reached, the gas flow was withdrawn gradually. In the final step, an upward-directed gas flow increased gradually to fluidize and break the powder bed under tension. As detailed in the result section, the tensile yield strength of the powder can be inferred from the pressure drop across the bed during the breaking process. Each test was repeated 3 times to assess the reproducibility of the results.

3. Results

Fig. 4 shows typical examples of the evolution of the pressure drop through the powder bed Δp (expressed as a non-dimensional ratio to the powder weight per unit area, W) as the gas velocity was increased. Lines represent different experiments where powder samples were subjected to pre-consolidation stresses (σ_c) up to 2 kPa. Initially, the gas pressure drop increases at a constant rate with the superficial gas velocity ($s = \Delta p/v_g$). As captured in the Carman–Kozeny relation, the passage of a viscous fluid through a granular bed induces a pressure drop proportional to the gas velocity at low Reynolds numbers [69]:

$$\frac{\Delta p}{h} = \frac{E\eta}{\psi_p^2 d_p^2}\frac{\phi^2}{(1-\phi)^3}v_g, \tag{1}$$

where E stands for the Ergun's empirical constant ($E \approx 180$), η refers to the gas dynamic viscosity, ψ_p is the particle's sphericity, h is the bed height, and ϕ is the particle volume fraction.

The point at which the pressure drop across the bed balances its weight per unit area ($\Delta p/W = 1$) defines the minimum gas fluidization velocity, v_{mf}. Beyond this critical point, the increase in the gas velocity would lead to a bubbling fluid-like regime in a noncohesive granular material. In these conditions, as the airflow drag matches the powder weight, particles lift, and the pressure drop would fluctuate around the weight per unit area. Fig. 4 reveals then the cohesive character of limestone powders since the pressure drop exhibits a linear trend that overcomes the v_{mf} threshold. Interparticle adhesive forces are strong enough to hold particles together, even when the pressure drop is larger than the powder weight. As this linear rate goes further, the competition between adhesion and drag forces tensions the powder progressively. As a result, powders break eventually when the over-pressure is equivalent to the tensile yield strength of the powder. Throughout the experiments, the fracture was triggered in a horizontal
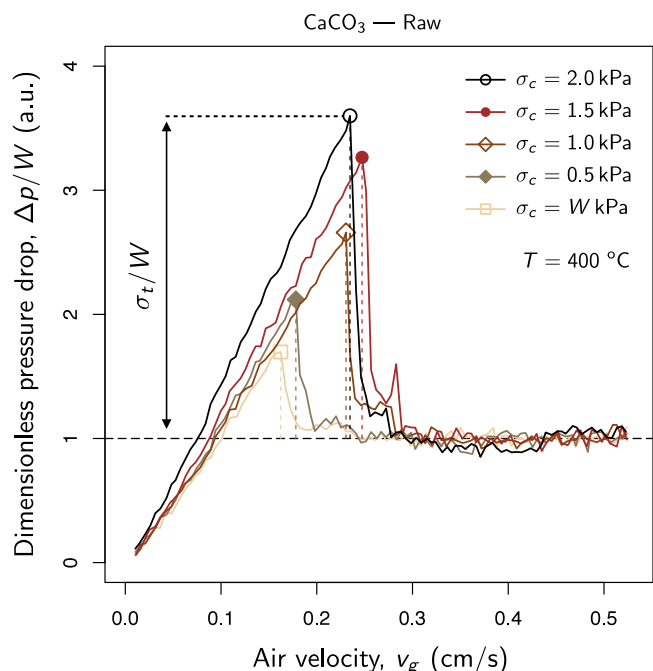
Fig. 4. Gas pressure drop, Δp, measured through the powder bed (expressed as a non-dimensional ratio to the powder weight per unit area, W) as a function of the gas velocity, v_g. Experiments were performed in fine limestone powder (raw, $CaCO_3$) at $T = 400\,°C$. Powder samples were subjected to different consolidation stresses previous to the fluidization cycle used to measure the tensile yield strength, σ_t. The pressure overshoot above the weight per unit area is used as a measure of the tensile yield strength of the powder.

Fig. 5. Gas pressure drop, Δp, measured through the powder bed (expressed as a non-dimensional ratio to the powder weight per unit area, W) as a function of the gas velocity, v_g. Experiments were performed in fine limestone powders (raw, $CaCO_3$) at different temperatures ranging from $30\,°C$ to $500\,°C$. Powder samples were previously subjected to a consolidation stress of $\sigma_c = 1500\,Pa$.

plane close to the bottom of the bed where the tensile stress reaches its maximum, as predicted theoretically [70–72].

After the peak, Δp falls abruptly to a value of around the weight per unit area. The overshoot in the pressure drop determines the tensile yield strength of the powder: $\sigma_t = \Delta p_{\max} - W$ (Fig. 4). This approximation assumes that wall retention effects do not introduce a significant contribution to the pressure drop. To control these effects, experiments were performed with a bed height always below its diameter [39].

Fig. 4 details the consolidation effect at $400\,°C$. Samples were subjected to different pre-loads by a downward-directed gas flow rate. According to Fig. 4, higher consolidation stresses lead to larger slopes through the linear stage $\Delta p/v_g$, which indicates that particles were packed in tighter structures of higher particle volume fraction. Furthermore, as consolidation increased, the tensile yield strength registered a significant increase too. As it shall be discussed later, loading particles enhance adhesion forces, which promotes the rise observed in the tensile yield strength. Similar trends have been reported in previous works on fine limestone at high temperatures [6,8], detailing how the cross-effect between temperature and consolidation modulates the tensile yield strength.

Fig. 5 shows the effect of temperature in the tensile yield strength when the samples were previously subjected to a consolidation stress of $\sigma_c = 1500\,Pa$. As it may be observed, the tensile yield strength increased significantly as temperature raised, which indicates that attractive forces between particles were increased accordingly. Besides, the initial slope, $\Delta p/v_g$, increased with temperature too. Gas viscosity could explain this rise in the slope since it goes from $16.08 \cdot 10^{-6}\,m^2/s$ at ambient temperature to $78.06 \cdot 10^{-6}\,m^2/s$ at $500\,°C$. A factor that might conceal the reduction in the particle volume fraction, as observed in previous studies [9,42]. In addition, Fig. 5 can be compared with Fig. 6, where the isotherm series were performed in limestone coated with nanosilica at $0.82\,wt\%$. Both figures exhibit similar trends, though the peaks were shifted to lower velocity in those samples coated with
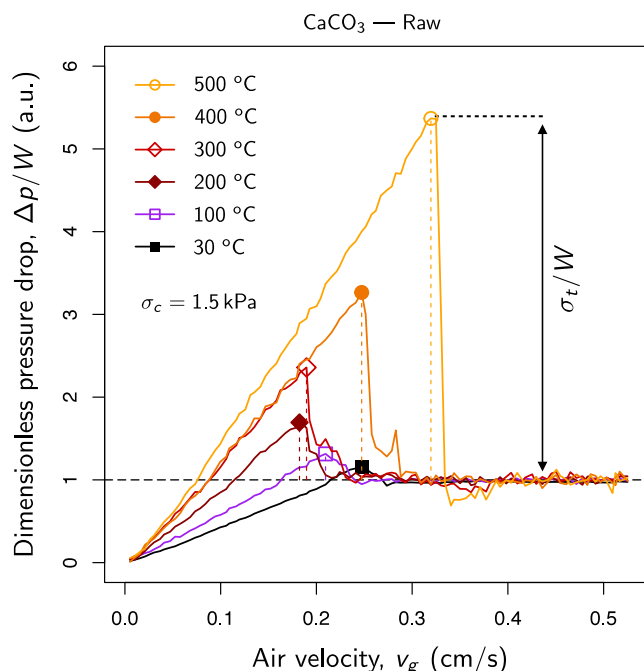
nanosilica. This shift evidences that nanosilica eases the fluidization regime in fine limestone powders.

Fig. 7 outlines the effect of the nanosilica content in the tensile yield strength for a given isotherm, $T = 400\,°C$. These experiments were conducted pre-loading the powder samples at $\sigma_c = 1\,kPa$. Interestingly, even when the samples were coated with a small amount of nanosilica, the tensile yield strength declined significantly. The largest drop is observed for nanosilica content above $0.6\,wt\%$, which would arguably yield a sufficiently high nanosilica coating level on the surface of the host limestone particles [20,42]. With particles coated uniformly, the contact between particles mostly happens via nanosilica aggregates. Regarding the initial slope $\Delta p/v_g$, it increased with the nanosilica content as the peaks shifted to lower velocities. According to Eq. (1), a reduction of interparticle attractive forces may explain this effect. As cohesion is reduced, particles could settle in tighter structures with larger particle volume fractions.

Fig. 8 shows how nanosilica can buffer the effect of the consolidation stress applied to the sample. In contrast to Fig. 4, doubling the consolidation stress at $400\,°C$ had no impact in the tensile yield strength when the nanosilica content was above $0.6\,wt\%$. At $500\,°C$ (Fig. 9), the nanosilica effect appears slightly less sharp than what is observed at $400\,°C$. Even though, nanosilica still reduced the tensile yield strength significantly compared to those values registered in raw limestone powders (Fig. 5).

The interested reader may check in the supplementary information a video showing the breaking of the bed with an animation on the simultaneous evolution of the gas pressure drop with the gas velocity at different temperatures. These videos illustrate the breaking of the bed near the bottom while the pressure drop falls abruptly. The notable increase of cohesiveness with temperature can be appreciated.
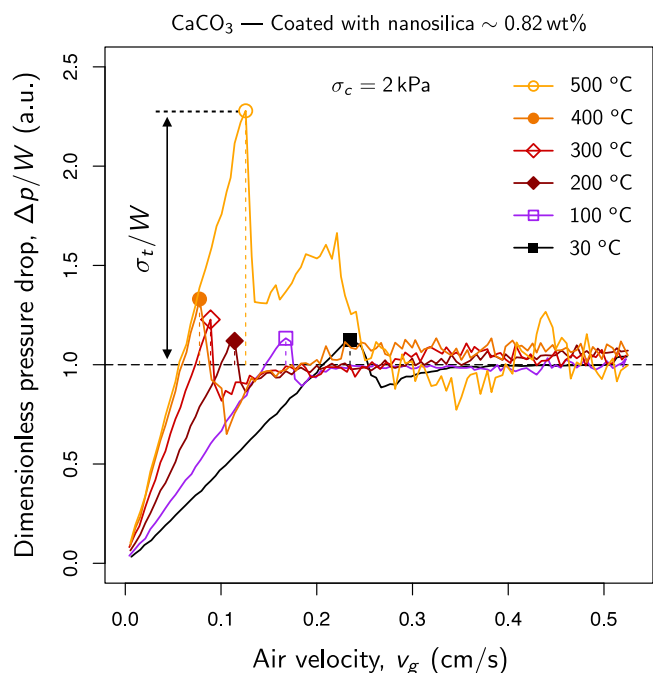
Fig. 6. Gas pressure drop, Δp, across the powder bed (expressed as a non-dimensional ratio to the powder weight per unit area, W) as a function of the gas velocity, v_g. Experiments were performed on fine limestone powder coated with nanosilica at 0.82 wt%. Coated samples were subjected to a consolidation stress of $\sigma_c = 2000$ Pa previous to the fluidization cycle used to measure the tensile yield strength. Each line represents an isotherm series ranging from 30 °C to 500 °C.
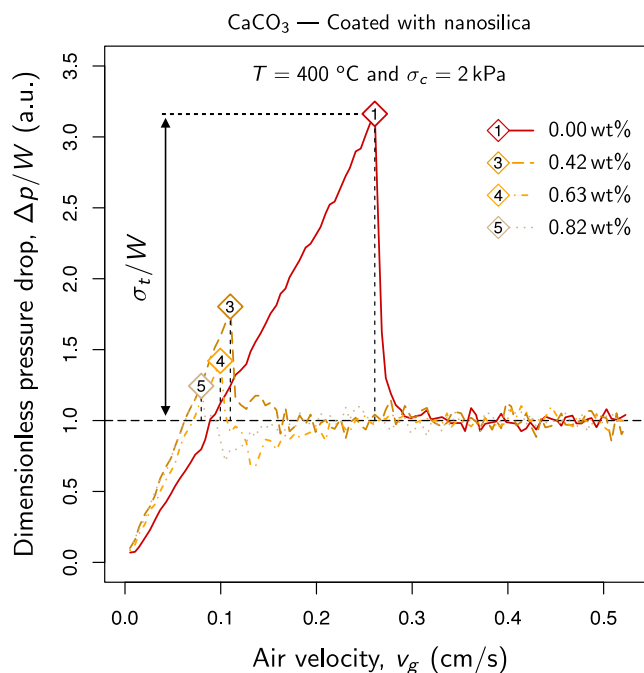

Fig. 8. Gas pressure drop, Δp, measured through the powder bed (expressed as a non-dimensional ratio to the powder weight per unit area, W) as a function of the gas velocity, v_g. Experiments were performed on fine limestone powder coated with nanosilica at different weight ratios from 0 wt% to 0.82 wt%. Samples were subjected to a consolidation stress of $\sigma_c = 2000$ Pa at $T = 400$ °C previous to the fluidization cycle used to measure the tensile yield strength.

Fig. 7. The gas pressure drop, Δp, measured through the powder bed (expressed as a non-dimensional ratio to the powder weight per unit area, W) as a function of the gas velocity, v_g. Experiments were performed on fine limestone powder coated with nanosilica at different weight ratios from 0 wt% to 0.82 wt%. Samples were subjected to a consolidation stress of $\sigma_c = 1000$ Pa at $T = 400$ °C previous to the fluidization cycle used to measure the tensile yield strength.
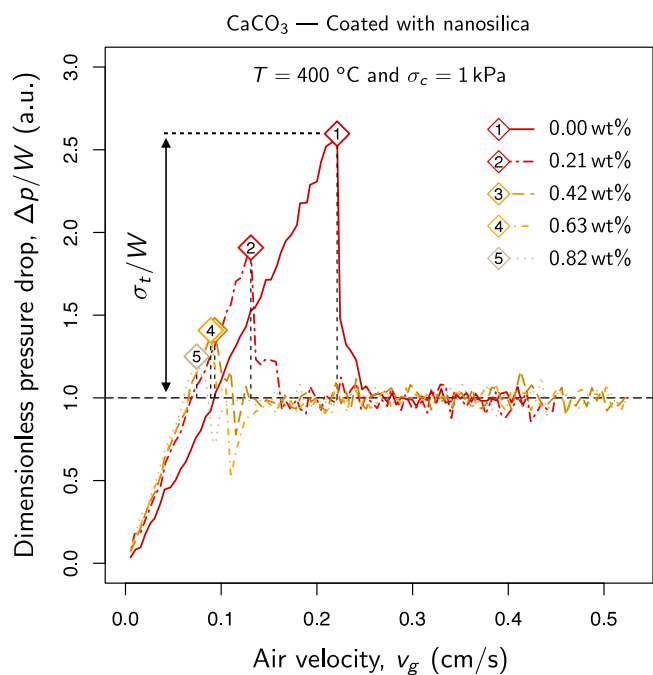

Fig. 9. Gas pressure drop, Δp, measured through the powder bed (expressed as a non-dimensional ratio to the powder weight per unit area, W) as a function of the gas velocity, v_g. Experiments were performed on fine limestone powder coated with nanosilica at different weight ratios from 0 wt% to 0.82 wt%. Samples were subjected to a consolidation stress of $\sigma_c = 1500$ Pa at $T = 500$ °C previous to the fluidization cycle used to measure the tensile yield strength.
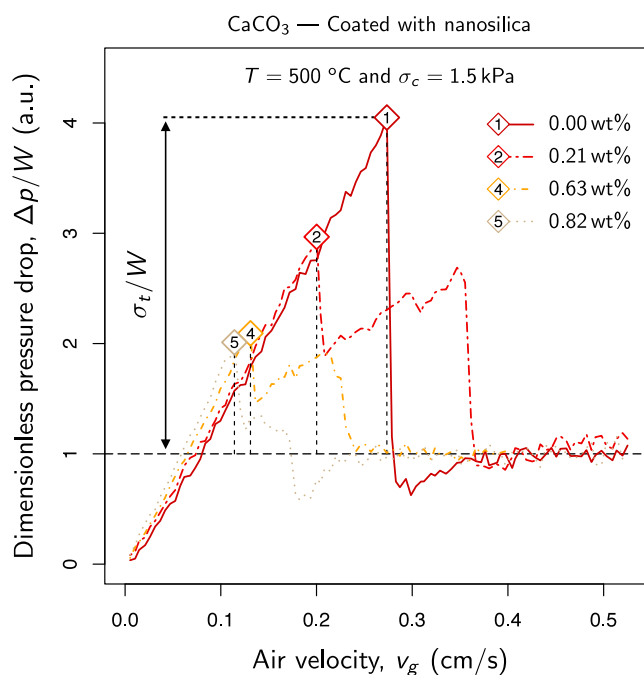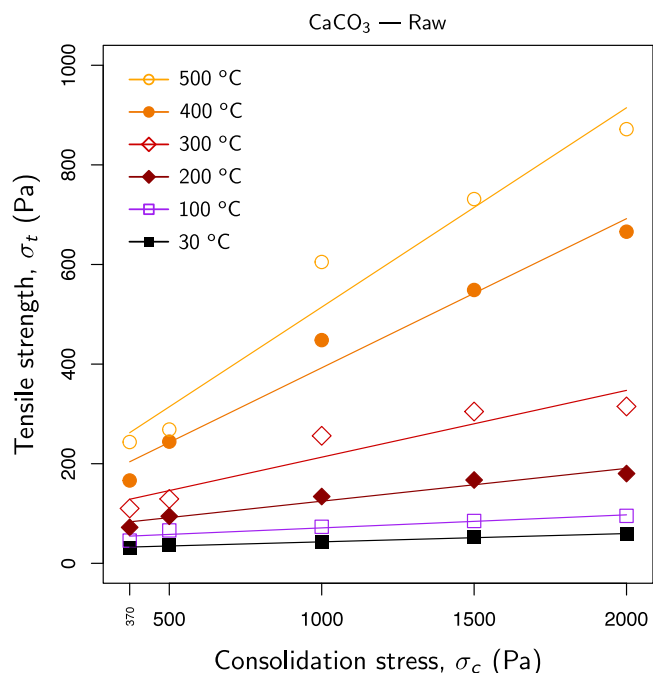
Fig. 10. Tensile yield strength of the powder bed, σ_t, as a function of the pre-consolidation stress, σ_c, for different isotherms. Raw sample of fine limestone powder were used in these series. Solid lines represent a linear fitting, although a more accurate regression model detailing the interaction between consolidation and temperature can be found in the Refs. [6,8].

3.1. Effect of temperature, pre-consolidation stress, and nanosilica content in the tensile yield strength

Fig. 10 represents the tensile yield strength as a function of the consolidation stress in the range of temperatures between ambient ($T = 30\,°C$) and $T = 500\,°C$. Data were derived from the fluidization curves for limestone samples. Fig. 10 maps the evolution of the peak in Fig. 4, showing that the tensile yield strength raised as the consolidation stress was increased. A similar trend can be inferred for the relationship between the tensile yield strength and the temperature mapping the evolution in Fig. 5. Both parameters, temperature and consolidation, led to an increase in σ_t, but interestingly they seem to reinforce each other from 300 °C. Fig. 10 shows a good agreement regarding how the interaction of these two parameters modulate the tensile yield strength as reported in the literature [6,8]. As described in previous works, from 300 °C consolidation shapes better contacts in fine limestone powders.

Analyzing the experimental data in Fig. 10, the tensile strength fits a linear regression model with the consolidation stress for a given isotherm:

$$\sigma_t(T) = a(T)\sigma_c + b(T), \tag{2}$$

where $b(T)$ represents the tensile strength in the absence of previous consolidation at a given temperature, which results in a negligible value compared to the powder weight per unit area (W). The constant rate in Eq. (2), $a(T)$, increases as the temperature raises, revealing higher degree of cohesion for similar consolidation stresses at high temperatures. In fact, σ_t exhibited an increase of two orders of magnitude for $\sigma_c = 2000\,Pa$ when the temperature was raised from 30 °C to 500 °C.

Fig. 11 outlines the central issue of this work, namely, how the use of nanosilica can alleviate the impact of temperature and consolidation in the tensile strength of fine limestone. At higher temperature, close to the Tamman temperature in limestone (Fig. 11,right), a nanosilica coating of 0.82 wt% induced a reduction factor around 3. The effect is equivalent to an effective temperature in the material of 200 °C below

the actual one, as it can be inferred contrasting the graphs at 300 °C and 500 °C in Fig. 11. Therefore, nanosilica coating offers an effective route to mitigate the impact of temperature and consolidation at high temperatures, even when added in small amounts (less than 1 wt%). These outcomes can be of interest in applications where limestone powders must be transported and stored at high temperatures such as the CaL process.

So far, the results have shown that coating limestone particles with nanosilica reduces cohesion forces significantly, although its impact on the powder flowability is not quantified yet. To that end, the so-called flow factor (ff) is used in the next analysis. This factor is commonly employed in the powder technology literature [73,74]. The flow factor is usually defined using unconfined yield strength data from shear testers; it prescribes the ratio between the consolidation stress used to pre-load the sample and the unconfined yield strength of the powder. A value of $ff < 4$ is considered as representative of a poorly flowing cohesive powder, whereas for $ff < 2$ the powder behaves as very cohesive. Admittedly, this work measured the tensile yield strength while the powder samples were subject to uniaxial tensile stresses. It is expected, though, that these measurements present similar values to those registered in yield stresses under shear for the same consolidations [75,76]. In these circumstances, an effective flow factor ff^* can be defined as the ratio between the consolidation stress imposed previously to the sample and the tensile yield strength of the powder ($ff^* = \sigma_c/\sigma_t$). According to the linear trend shown by the experimental data (Eq. (2)), the flow factor result in $ff^* \approx 1/a$ for the range of consolidation stresses explored in this work.

Fig. 12 shows how the content of nanosilica (wt%) alters the powder flowability throughout different isotherms. In the absence of additive, the limestone powder tested in this work (average particle size $d_p = 45\,\mu m$) exhibited a free flowing behavior at ambient temperature. However, above 300 °C approximately, the free flowing behavior was turned into cohesive in the absence of nanosilica. At $T = 500\,°C$ with 0 wt% content of nanosilica, the flow factor reached similar values to those observed in very cohesive fine limestone powders with particle size around $d_p = 4.6\,\mu m$ at ambient temperature (reported elsewhere [77]). Therefore, Fig. 12 indicates how the use of nanosilica in fine limestone powder boosts the limestone flowability at high temperatures, keeping the samples within the free-flowing regime when nanosilica content is above 0.6 wt%.

3.2. Effect of temperature, pre-consolidation stress, and nanosilica content in the packing fraction

The particle volume fraction (or packing fraction ϕ) for a consolidated bed can be measured at room temperature using ultrasonic sensors (original SPT device [71,72]). This technique consists primarily of measuring the height of the bed, which is used to calculate the particle volume fraction. Unfortunately, this technique introduces a technical limitations as the sensor cannot operate at high temperatures. The Carman–Kozeny equation (Eq. (1)) offers an alternative for an indirect measurement of the particles volume fraction. In effect, from the linear stage in the fluidization curves, the slope $\Delta p/v_g$ relates to the unknown parameter: the ratio E/ψ_p^2, which depends on the particles' shape. This factor, however, is not sensitive to temperature [78] and could be estimated using the volume fraction at ambient temperature obtained by ultrasonic sensors.

Thus, fitting the linear stage of the experimental data to the Carman–Kozeny equation, the ratio resulted in $E/\psi \approx 272$, which is close to values reported in the literature [78] for particles with irregular shapes. In fact, SEM images (Fig. 1,2) show that (1) limestone particles used in this work exhibit irregular shapes, and (2) shapes are not visibly affected by temperature. As a result, the ratio E/ψ_p^2 can be considered constant for limestone below 500 °C, which makes possible to estimate the particle volume fraction of the pre-consolidated bed by a linear fitting through the pre-peak region.
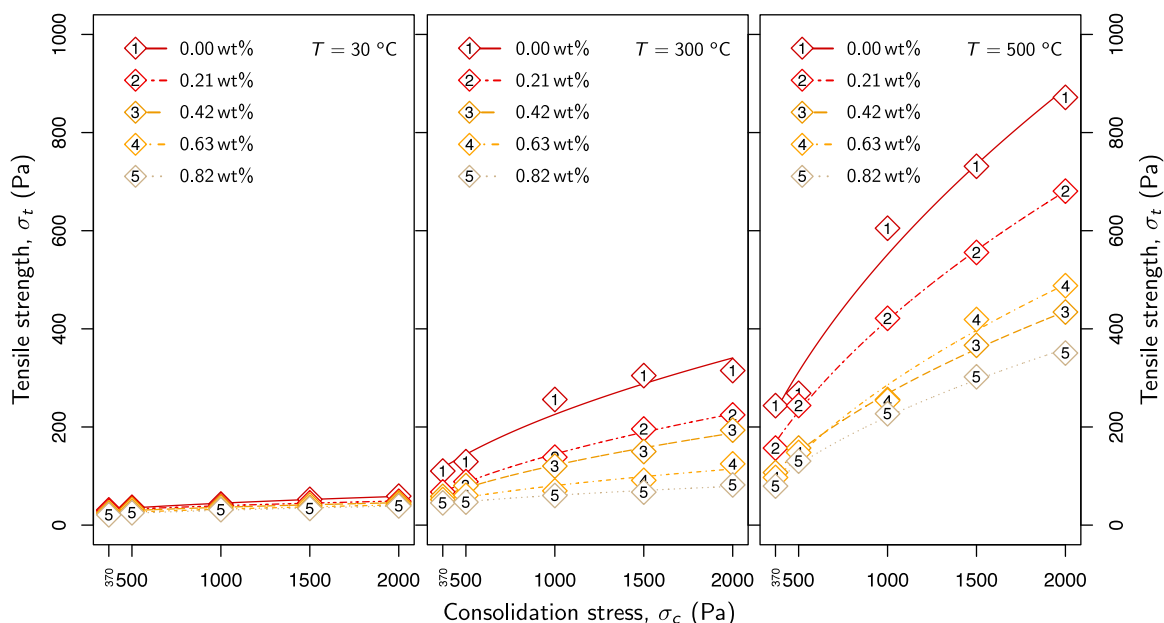
Fig. 11. Effect of nanosilica coating in tensile yield strength, σ_t, as temperature increases from 30 °C to 500 °C. Solid lines fit the experimental data according to the interaction between consolidation and temperature [6,8].
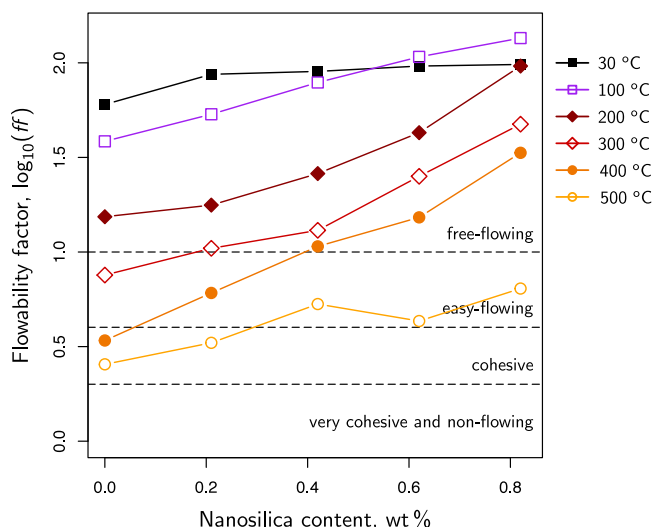

Fig. 12. Effective flow factor, ff^*, as a function of the nanosilica content, wt%, throughout different isotherms.

Fig. 13 illustrates the effect of nanosilica coating in the volume fraction through different isotherms ranging from 30 °C to 500 °C. The volume fractions, ϕ, were considerably below the theoretical limit for the random loose packing of hard non-cohesive spheres even in the absence of consolidation stresses ($\phi_{RLP} \approx 0.55$ [79]). This because of the limestone powder cohesiveness and the irregular shapes of the particles. Data fits to the type logarithmic law $\phi = c + d \ln \sigma_c$ used in previous studies [9,42] for other fine cohesive powders.

On the other hand, Fig. 13 highlights that temperature reduced the particle volume fraction. This effect maps the increase in the powder cohesiveness, which hinders the particles mobility preventing thus tighter structures. The increase of ϕ with σ_c becomes more prominent at higher temperatures. Variations were more steep in fine limestone powders without additives (Fig. 13, left). For instance, for consolidation stresses in the interval between W and 1000 Pa, ϕ registered an increase around 3%, approximately at $T = 30$ °C, whereas ϕ increased

by a 14% at 500 °C. Fig. 13 shows how the use of nanosilica leads to larger values of ϕ (Fig. 13, right). This is because of nanosilica reduces interparticle attractive forces, easing then that particles pack in closer arrangements. For a 0.82 wt% of nanosilica, the particle volume fraction was decreased significantly only when coated samples were heated up to 500 °C. In contrast, below 500 °C the variations in ϕ were negligible, indicating that nanosilica help to set a stable internal powder structure for a broad range to temperatures (Fig. 13, right).

4. Discussion

4.1. Powder cohesiveness at small consolidation stresses

Cohesive Bond number [80] compares attractive forces F_{at} between particles with their weight mg:

$$Bo_g = \frac{F_{at}}{mg}. \tag{3}$$

If $Bo_g \ll 1$, adhesion forces between particles are negligible. Particles, then, may flow freely if the drag is strong enough to lift them up. As attractive forces between the particles prevail over their weight, powder cohesiveness becomes appreciable. Flowability is then hindered due to particle aggregation [7].

In the absence of humidity and external fields, attractive interparticle forces are determined mainly by the ubiquitous van der Waals force. By neglecting retardation effects and assuming pairwise dipole–dipole interaction, the van der Waals force between two unloaded particles at contact is given by [81]:

$$F_{vdW} \approx \frac{A D^*}{20 z_0^2}, \tag{4}$$

where A refers to the Hamaker constant, whose typical value for most solids in vacuum is about 10^{-19} J; z_0 is the minimum distance between the solids which ranges from 3 to 5 Å; and $D^* = 2R^*$, where R^* is the reduced local radius of curvature of the surfaces at contact.

Since the van der Waals force is a short-ranged interaction, its magnitude is very sensitive to the roughness of the contact surfaces. Thus, for particles with irregular shapes, as those used in this study, the typical size of asperities must be employed for D^* in Eq. (4) [81].
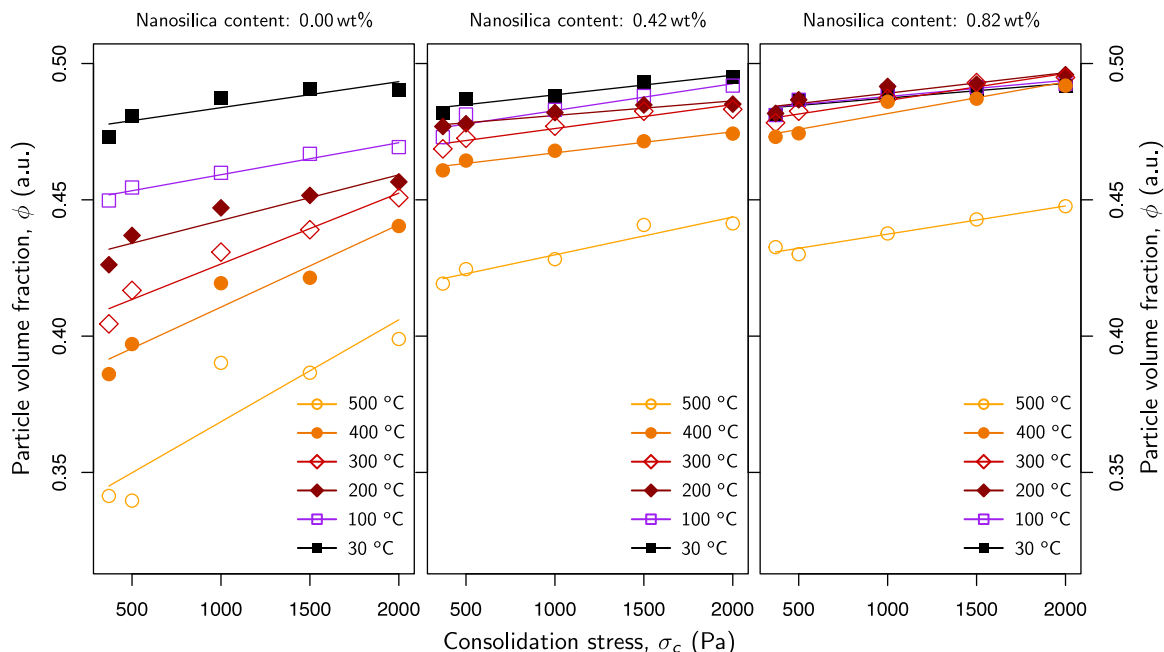
Fig. 13. Particle volume fraction of the powder bed, ϕ, as a function of the consolidation stress, σ_c. Nanosilica content varies from 0 (raw samples) to 0.82 wt% for each isotherm series where temperatures ranges from 30 °C to 500 °C. The solid lines represent the fitting according to the equation $\phi = d + \ln \sigma_c$.

This parameter has a typical value $d_{\mathrm{asp}} \approx 0.2\,\mu m$ for most powders [75]. Hence, the granular Bond number may be expressed as:

$$\mathrm{Bo}_g = \frac{3 A d_{\mathrm{asp}}}{20 \pi g z_0^2 \rho_p d_p^3}. \tag{5}$$

According to Eq. (5), powder cohesiveness increases rapidly as particle size decreases. In particular, for the fine limestone powder used in this work ($d_p = 45\,\mu m$) $\mathrm{Bo}_g \approx 1$. Thus, the cohesiveness of this powder at low consolidations and ambient temperature is not relevant as observed experimentally. Moreover, it would not be critically affected by the increase of temperature since the van der Waals force increases only weakly with temperature [78] through the Hamaker constant. As seen in Fig. 10, extrapolation of the experimental data to very low consolidations yields accordingly very low values of the tensile yield strength. Moreover, there is not a relevant effect of temperature as expected. However, the tensile yield strength measured in this work, which is an average measure of the interparticle attractive forces, is notably increased as the powder was subjected to larger consolidation stresses. As the powder cohesiveness increases, its flowability reduces which is a serious issue to transport the granular material through the storage unit. This issue would be aggravated as temperature gets closer to the Tamman temperature in limestone (~ 545 °C) [82]. These observations are relevant within the context of the Ca-looping process, where the powder may be subjected to high consolidation stresses during storage at conditions that may involve temperatures on this order or even higher [83].

The experimental results presented above demonstrate that nanosilica coverage serves to mitigate the increase of the powder tensile yield strength with consolidation and temperature, improving the powder flowability. However, Eq. (4) cannot explain the appreciable increase of the tensile yield strength with consolidation and temperature because when interparticle contacts are loaded the adhesion between particles is not determined anymore by the van der Waal force between unloaded particles. It is therefore necessary to assess the physical mechanisms that govern the adhesion between particles under load in order to devise possible solutions to mitigate the augmentation of powder cohesiveness with consolidation and temperature.

4.2. Adhesion force between particles under load

The cohesiveness of pre-consolidated powders and, consequently, their flowability is ultimately determined by the microscopic forces required to separate the loaded particles F_t (so-called pull-off or interparticle adhesion force). If the particles are subjected to small loads, the contact is usually elastic [84,85]. In this regime, the imposed external load has no remarkable effect on the adhesion forces. The elastic limit is exceeded when the load force reaches a critical value that depends on the solid physical properties. Then, a region of the solid in the vicinity of the contact point deforms plastically. As the load force is raised above the threshold value, the plastic zone spreads inside the bulk of the solid until, eventually, reaches the contact surface and propagates along it [20].

The interparticle adhesion force in the elastic–plastic regime is determined by the indentation and decohesion stages [20]. During the indentation stage, the solid deforms plastically as the external load force F_c is applied. In the following decohesion stage, it arrives a point at which the attractive force between the solids at contact is overcome. Then, the particles recover their profile when the contact is broken. The critical value of the pull-off force to break the contact F_t depends on the previously applied load force and on the mechanical properties of the solids at contact [86–88].

For a frictionless contact between an elastic–plastic sphere and a rigid flat surface, Mesarovic and Johnson obtained F_t as:

$$F_t = s_{EP} \sqrt{F_c} = \lambda \frac{2 w E^*}{(\pi H^3)^{1/2}} \sqrt{F_c}, \tag{6}$$

Here H is the solid hardness (when dissimilar materials are at contact the relevant hardness is that of the softer material) [44], w is the work of adhesion between the solid surfaces defined as the work required to separate two half-spaces to infinity in vacuum ($w = 2\gamma$ for two surfaces of the same material where γ is the particle surface energy), E^* denotes the reduced Young's modulus,

$$E^* = \left[\frac{1 - \nu_1^2}{E_1} + \frac{1 - \nu_2^2}{E_2} \right]^{-1} \tag{7}$$

with ν_i and E_i the Poisson ratio and the Young's modulus, respectively, of the solids ($i = 1, 2$) at contact, and λ is a parameter depending on

the dimensionless Tabor number μ[89]:

$$\mu = \left(\frac{d_{asp}^* w^2}{2z_0^3 E^{*2}}\right)^{1/3}.$$ (8)

In the Derjaguin, Muller and Toporov –DMT– limit [90] ($\mu \ll 1$) it is $\lambda = 1$ whereas for $\mu \gg 1$ (Johnson, Kendal and Roberts – JKR– limit [88]) it is $\lambda = 3/4$. Using the central values reported for CaCO$_3$ mechanical properties (Table 1) the Tabor number at room temperature can be estimated as $\mu = 0.77$, which is in between the JKR and DMT limits. The interested reader may see further details in [20,86,87,91,92].

To determine which type of deformation exists between the solids at contact (either purely elastic or elastic–plastic), it is necessary first to calculate the Tabor number, and then estimate when the onset of plastic behavior and ultimately the onset of fully plastic regime would occur.

For $\mu \gg 1$, the JKR theory states that the onset of plasticity, considering only the effect of attractive forces, is established when the reduced radius of asperities at contact $d_{asp}^*/2$ is smaller than [20,93]

$$R_P^{JKR} = \frac{M_0^3}{\pi^2}\left(\frac{w E^{*2}}{Y^3}\right),$$ (9)

being $M_0 \approx 0.447$ for $v = 0.28$ and $Y = H/2.8$.

Meanwhile, for $\lambda \ll 1$, in the DMT model, assuming that the forces are determined by the Hertz solution, the solids at contact start to flow plastically when $d_{asp}^*/2$ is below [20,94]

$$R_P^{DMT} = \frac{12 w E^{*2}}{\pi^2 K^3 Y^3},$$ (10)

with $K = 1.271 + 1.148v$. Since the estimated Tabor number in the case studied, $\mu = 0.77$, is between the limits of validity of the JKR and DMT models, the value of the reduced radius, should lie between the values estimated from both models. Eq. (9)–(10) yield $R_P^{JKR} = 1.77\,\mu m$ and $R_P^{DMT} = 1.64\,\mu m$ using the central values of the mechanical properties values illustrated in Table 1. These threshold values are both higher than the typical asperity size ($d_{asp}^*/2 \approx 0.1\,\mu m$ [95,96]), thus it may be assumed that limestone particles at contact experience plastic deformation when loaded and Eq. (6) is a roughly valid estimation for the inter-particle adhesion force.

Eventually the contact would reach the fully plastic regime as the load force is increased, and the plastic zone spreads to reach the whole contact surface. In this regime, Chowdhury et al. assumed that deformation is sustained solely by one sphere undergoing a compressive force Fc against a rigid plane [97]. The resulting pressure is homogeneously distributed on the contact area and is given by $F_c = \pi a^2 H$ at the end of the indentation stage, where a is the radius of the contact area. Maugis and Pollock stated that the contact reaches full plasticity if $P + 2\pi w d_{asp}^* = \pi a_p^2 H$ with $a_p \approx (30 d_{asp} Y)/E^*$ and P is the load. Based on this approximation, Castellanos [20] determined the onset of full plasticity for a threshold radius given by:

$$R_{MP}^{FP} = \frac{\pi w + \sqrt{\pi^2 w^2 + AP}}{A},$$ (11)

where $A \approx \pi 10^4 Y^3/E^2$.

Eq. (11) leads to $R_{MP}^{FP} \approx 0.05\,\mu m$ using the CaCO$_3$ physical properties shown in Table 1, which is similar to the typical radius of asperities. Thus, it may be concluded that the contact between surface asperities is close to the threshold for the onset of full plasticity. Therefore, the contact between limestone powder particles would be situated between the elastic–plastic and fully plastic models. The adhesion force in the case of fully plastic contact with elastic recovery is then expressed as [20]

$$F_t = s_{EFP}\sqrt{F_c} = \lambda \frac{8 w E^*}{3(\pi H^3)^{1/2}}\sqrt{F_c}.$$ (12)

To discuss the experimental results based on the above equations, the microscopic interparticle contact forces must be estimated from the
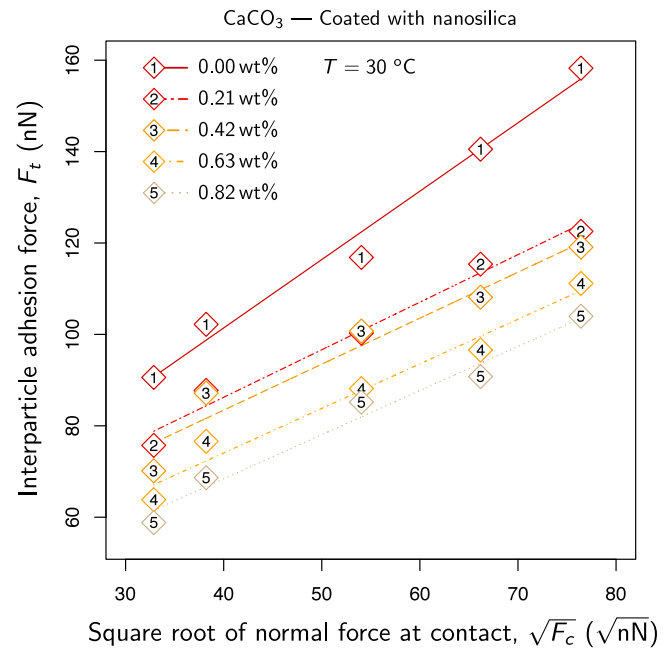

Fig. 14. Estimated interparticle adhesion force, F_t, as a function of the square root of the estimated consolidation force, F_c, from the tests carried out at ambient temperature for the limestone powder mixed with nanosilica at different weight ratios.

measured bulk stresses. To this end, the Rumpf averaging equation [98] employed in previous works for this purpose [9,42] can be used

$$F_i = \frac{\pi d_p^2}{\phi \xi}\sigma_i,$$ (13)

where F_i is the interparticle contact force (either consolidation or adhesion force) and σ_i is the measured stress (either tensile yield strength or consolidation stress), ϕ is the particle volume fraction and ξ is the coordination number (number of contacts per particle) which can be calculated from the particle volume fraction according to the relationship proposed by Nakagaki et al. [99]

$$\xi = \frac{\pi}{2}(1 - \phi)^{-3/2}.$$ (14)

Eq. (14) holds for $\phi > 0.18$ which fits the range of measured values in this work.

At ambient temperature, for CaCO$_3$ particles, using the central values of the mechanical properties reported in Table 1, a theoretical value of the slope $s_{EP} = F_t/\sqrt{F_c}$ may be calculated that lies between 3.42 and 4.56 $\sqrt{nN}$ for the JKR limit ($\lambda = 3/4$) and the DMT limit ($\lambda = 1$), respectively. On the other hand, for s_{EFP}, its value ranges from 4.6 to 6.1 for fully plastic contacts with elastic recovery. Fig. 14 shows data on the estimated interparticle adhesion force as a function of the square root of the estimated interparticle load force for the samples with different weight ratios of added nanosilica and tested at ambient temperature. As can be seen, the data is well fitted by a linear law ($F_t = s_{exp}\sqrt{F_c} + e$). The experimental slope in the absence of nanosilica is $s_{exp} = 1.6$ which is on the same order of magnitude than the theoretical expectations for both values estimated above (s_{EP} and s_{EFP}).

It must be noted that the above calculations are subject to different sources of indeterminacy that do not allow for more precise quantitative estimations. As can be noticed in Table 1, the mechanical properties of CaCO$_3$ are not accurately determined which adds uncertainty to the estimated value of s_{EP}. Furthermore, the use of Rumpf equation in order to calculate the contact forces can be considered only as a rough approximation as it is strictly valid just for a random isotropic packing of hard, monodisperse and perfectly spherical particles. In contrast, the powders tested in this study consist of particles of

irregular shape, and their packing is not perfectly isotropic, albeit they show a reduced size dispersion. In addition, the theory on contact forces holds only for the case of a single interparticle contact. In practice contacts would occur most likely at several points comprising multiple asperities. Despite all these issues, the acceptable agreement between the experimental value of s_{exp} and the theoretical expectations at ambient temperature yields confidence to the results presented in this work and the technique employed for measurement. In the next section the effects of nanosilica coating and temperature on interparticle contact forces are analyzed to get a grip on the observed effects of these parameters on the powder tensile yield strength (Fig. 11).

4.3. Effects of nanosilica surface coating and temperature on interparticle forces

Figs. 1,2 show some SEM images of the $CaCO_3$ powders used in this study mixed with nanosilica (by 0.42 and 0.82 wt%). These SEM images indicate that the simple rotating drum technique employed in this work for nanosilica surface coating is an efficient method to obtain a rather homogeneous coating of the limestone particles. As can be observed, silica nanoparticle aggregates of size on the order of 100 nm appear uniformly dispersed on the $CaCO_3$ particles surface. As discussed in previous studies these primary aggregates are formed during the production of the nanosilica powder (Aerosil R974 from Evonik), which consists of flame synthesis causing the fusion of nanoparticles in these small permanent aggregates [100,101].

Limestone particles become increasingly coated as the nanosilica wt% is increased. SEM images indicate that for the highest nanosilica wt% employed, the coating remains uniform and extends over most of the host limestone particle surface. Plausibly, strong triboelectric forces of attraction arise between the guest nanosilica aggregates and the host limestone particles during mixing since both materials are placed in distant extremes of the triboelectric series [102]. These electrostatic forces between the dissimilar materials would lead to the observed uniform coating and would preclude the detachment of the nanosilica aggregates form the limestone particles during handling [102].

The contact between limestone particles coated with different amounts of nanosilica may occur between limestone asperities (p–p contact), between limestone asperities and nanosilica aggregates (p–a contact) or between nanosilica aggregates (a–a contact). As the nanosilica wt% is increased the predominant type of contact would gradually shift from p–p contact to a–a contact. When the prevailing type of contact is p–a, the theoretically expected slopes s_{EP} and s_{EFP} are changed since the reduced Young's modulus and the work of adhesion depend on the mechanical properties of the dissimilar materials at contact. To estimate the expected slope, the central values of the mechanical properties provided in Table 1 for $CaCO_3$ and SiO_2 may be used, leading to a value of s_{EP} (p–a contact) in a range between 0.52 and 0.69 $\sqrt{nN}$ while the values of s_{EFP} (p–a contact) are between 0.7 and 0.93 $\sqrt{nN}$. The lowest limit in these intervals corresponds to the JKR approximation and the highest one to the DMT limit.

As the surface coverage of nanosilica is increased over a sufficiently high value, most of interparticle contacts would be established between nanosilica aggregates (a–a contact). In this case, the slopes s_{EP} and s_{EFP} would depend only on the mechanical properties of silica. Using the mechanical properties reported in Table 1 for silica at ambient temperature, the value calculated for s_{EP} (a–a) lies between 0.11 and 0.15 $\sqrt{nN}$ (Eq. (6)) whereas s_{EFP} (a–a) ranges between 0.15 and 0.20 $\sqrt{nN}$ (Eq. (12)). Consequently, it is expected that nanosilica addition would significantly reduce the interparticle adhesion force mainly due to the increase of hardness (from $H \approx 2.93 \cdot 10^9$ Pa for $CaCO_3$ to $H \approx 6 \cdot 10^9$ Pa for silica). The foregoing expressions and calculations are valid at room temperature. The values reported for s_{exp} for the different nanosilica concentrations are comprised between ~ 1.12 and 1.03 for the lowest and highest amounts of nanosilica, respectively,

which are close to the upper limit of the range predicted by the elastic–fully plastic model (0.93 $\sqrt{nN}$) for a p–a contact type. Thus, in the range of nanosilica wt% employed in this work most contacts would expectedly occur between an asperity of the host limestone particle and an aggregate of nanosilica. Indeed, it should be underlined that even though the theoretical models employed consider only a single (p–a) type contact, the experimental results of this work are in good agreement with the theoretical predictions.

Let us now turn the discussion to the effect of temperature on the interparticle forces when limestone particles are coated with nanosilica. Fig. 15 shows the estimated values of the contact forces as a function of temperature and nanosilica wt%. The solid lines correspond to the best linear fits to the data. As may be seen the experimental slopes s_{exp} are gradually decreased as the nanosilica wt% is increased. Even for the smallest nanosilica wt%, the slope values are appreciably smaller than those obtained for the raw limestone samples. This marked reduction would be explained by the transition of the predominant contact type to p–a contact and to a–a contact as the nanosilica wt% is further increased.

Remarkably, the favorable effect of nanosilica becomes more pronounced at higher temperatures ($T \gtrsim 300\,°C$). As the host limestone particles become increasingly coated with nanosilica, the slope is progressively decreased depending on temperature. These results should be explained based on the tradeoff between the decrease of mechanical hardness of materials with temperature on the one hand [103], and the increase of the contact hardness as the nanosilica surface coverage is increased on the other hand. Unfortunately, the reported data on the effect of temperature on the mechanical hardness of silica are scarce and spread. Michel. et al. [104] measured from indentation tests the hardness of fused nanosilica decreased from 7.3 GPa at room temperature to 4.2 GPa at 400 °C, which is in qualitative agreement with the results. Arguably, the decrease of silica hardness with temperature is not as significant as it is for limestone in the range of temperatures used in our tests since the Tamman temperature of silica ($T_{Tam} = 714\,°C$) is well above the limestone Tamman temperature ($T_{Tam} = 545\,°C$). Accordingly, nanosilica coating would be an efficient method to mitigate the notable increase of limestone cohesiveness with temperature as inferred from the results. On the other hand, the results found in literature indicate that the work of adhesion is almost independent on temperature [105]. Regarding the Young's modulus, experimental results show that it generally decreases with temperature, but no quantitative data has been found for the materials employed in this work [103,106–108]. Further research is needed about the dependence of these mechanical properties on temperature to find a quantitative prediction on the evolution of interparticle forces to be compared with experimental data.

5. Conclusions

In the present study, the effect of temperature on the cohesive behavior of a limestone powder (45 μm average particle size) has been investigated from experimental measurements of the tensile yield strength and compressibility as a function of the previously applied consolidation stress. This research is relevant for applications such as the Calcium Looping process wherein the flow of limestone based powders must be resumed after periods of storage at high temperature usually close to, or even above, the Tamman temperature. At ambient temperature, the cohesiveness of this powder is relatively small showing good flowability since the magnitude of interparticle adhesive forces is similar to particle weight. However, cohesiveness is significantly enhanced with temperature as the consolidation stress is increased, which hinders powder flowability. The main mechanism that drives this deleterious behavior is softening of the solids at contact, which greatly promotes interparticle adhesion. This work has been focused on analyzing the effect of nanosilica surface coating on the tensile yield strength and compressibility of the powder as temperature is raised.
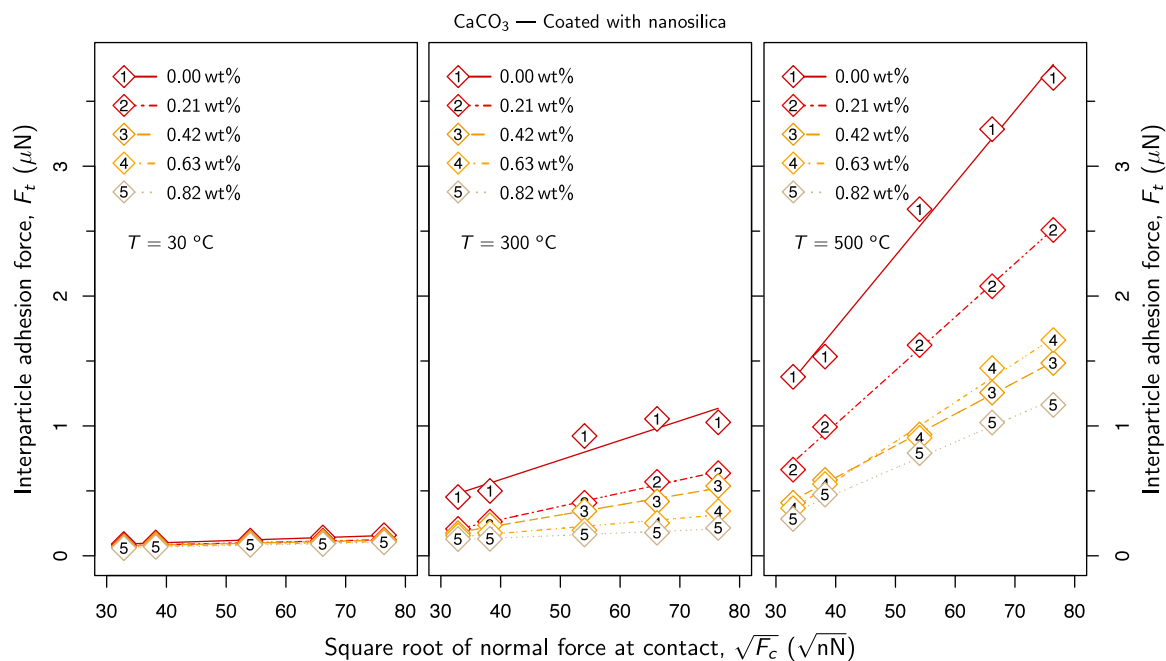
CaCO₃ — Coated with nanosilica

Fig. 15. Estimated interparticle adhesion force, F_t, as a function of the square root of the estimated interparticle consolidation force, F_c, from the tests carried out at different temperatures for the limestone powder mixed with nanosilica at different weight ratios.

The addition of nanosilica by small amounts (below 1 wt%) using a simple dry mixing method leads to a uniform coating of the surface of the limestone particles. Results show that nanosilica surface coating mitigates significantly the enhancement of powder cohesiveness with temperature thus improving flowability. A theoretical analysis based on contact mechanics indicates that the main physical mechanism responsible for this effect is the increase of contact hardness as the dominant type of interparticle contacts changes from $CaCO_3$ contacts to contacts between the nanosilica aggregates that coat the limestone particles. Therefore, it may be concluded that, in general, a potentially useful technique to circumvent the loss of powder flowability with temperature is to coat the powder particles using additives with enhanced thermal and mechanical resistance.

Declaration of competing interest

The authors declare that they have no known competing financial interests or personal relationships that could have appeared to influence the work reported in this paper.

Appendix A. Supplementary data

Supplementary material related to this article can be found online at https://doi.org/10.1016/j.cej.2021.131789.

References

[1] Pedro Pardo, Alexandre Deydier, Zoé Anxionnaz-Minvielle, Sylvie Rougé, Michel Cabassud, Patrick Cognet, A review on high temperature thermochemical heat energy storage, Renew. Sustain. Energy Rev. 32 (2014) 591–610.

[2] N.L. Panwar, S.C. Kaushik, Surendra Kothari, Role of renewable energy sources in environmental protection: a review, Renew. Sustain. Energy Rev. 15 (3) (2011) 1513–1524.

[3] Pablo Arce, Marc Medrano, Antoni Gil, Eduard Oró, Luisa F. Cabeza, Overview of thermal energy storage (TES) potential energy savings and climate change mitigation in Spain and Europe, Appl. Energy 88 (8) (2011) 2764–2774.

[4] Sarada Kuravi, Jamie Trahan, D. Yogi Goswami, Muhammad M. Rahman, Elias K. Stefanakos, Thermal energy storage technologies and systems for concentrating solar power plants, Prog. Energy Combust. Sci. 39 (4) (2013) 285–319.

[5] Cristina Prieto, Patrick Cooper, A. Inés Fernández, Luisa F. Cabeza, Review of technology: Thermochemical energy storage for concentrated solar power plants, Renew. Sustain. Energy Rev. 60 (2016) 909–929.

[6] F.J. Durán-Olivencia, J.M.P. Ebrí, M.J. Espín, J.M Valverde, The cohesive behavior of granular solids at high temperature in solar energy storage, Energy Convers. Manage. 240 (2021) 114217.

[7] A. Castellanos, J.M. Valverde, M.A.S. Quintanilla, Aggregation and sedimentation in gas-fluidized beds of cohesive powders, Phys. Rev. E 64 (4) (2001) 041304.

[8] F.J. Durán-Olivencia, M.J. Espín, J.M. Valverde, Cross effect between temperature and consolidation on the flow behavior of granular materials in thermal energy storage systems, Powder Technol. 363 (2020) 135–145.

[9] M.J. Espín, F.J. Durán-Olivencia, J.M. Valverde, Role of particle size on the cohesive behavior of limestone powders at high temperature, Chem. Eng. J. 391 (2020) 123520.

[10] E. Teunou, J.J. Fitzpatrick, E.C. Synnott, Characterisation of food powder flowability, J. Food Eng. 39 (1) (1999) 31–37.

[11] Qi Bian, Sichaya Sittipod, Anubha Garg, R.P. Kingsly Ambrose, Bulk flow properties of hard and soft wheat flours, J. Cereal Sci. 63 (2015) 88–94.

[12] A.K.H. Kwan, J.J. Chen, Adding fly ash microsphere to improve packing density, flowability and strength of cement paste, Powder Technol. 234 (2013) 19–25.

[13] R. Chacartegui, et al., Solar calcium-looping integration for thermo-chemical energy storage, in: Horizon 2020 – the EU Framework Programme for Research and Innovation, ref.3228/0666, https://cordis.europa.eu/project/rcn/212577_en.html.

[14] T. Shimizu, T. Hirama, H. Hosoda, K. Kitano, M. Inagaki, K. Tejima, A twin fluid-bed reactor for removal of CO_2 from combustion processes, Chem. Eng. Res. Des. 77 (1) (1999) 62–68.

[15] Ronald Barker, The reversibility of the reaction $CaCO_3 \rightleftharpoons CaO+CO_2$, J. Appl. Chem. Biotechnol. 23 (10) (1973) 733–742.

[16] Ronald Barker, The reactivity of calcium oxide towards carbon dioxide and its use for energy storage, J. Appl. Chem. Biotechnol. 24 (4–5) (1974) 221–227.

[17] Gilles Flamant, Daniel Hernandez, Claude Bonet, Jean-Pierre Traverse, Experimental aspects of the thermochemical conversion of solar energy; decarbonation of $CaCO_3$, Sol. Energy 24 (4) (1980) 385–395.

[18] Ricardo Chacartegui, A. Alovisio, C. Ortiz, J.M. Valverde, V. Verda, J.A. Becerra, Thermochemical energy storage of concentrated solar power by integration of the calcium looping process and a CO_2 power cycle, Appl. Energy 173 (2016) 589–605.

[19] C. Ortiz, J.M. Valverde, Ricardo Chacartegui, Luis A. Perez-Maqueda, P. Giménez, The calcium-looping ($CaCO_3$/CaO) process for thermochemical energy storage in concentrating solar power plants, Renew. Sustain. Energy Rev. 113 (2019) 109252.

[20] Antonio Castellanos, The relationship between attractive interparticle forces and bulk behaviour in dry and uncharged fine powders, Adv. Phys. 54 (4) (2005) 263–376.

[21] J. Carlos Abanades, Diego Alvarez, Conversion limits in the reaction of CO_2 with lime, Energy & Fuels 17 (2) (2003) 308–315.

[22] Gemma S. Grasa, J. Carlos Abanades, Mónica Alonso, Belén González, Reactivity of highly cycled particles of CaO in a carbonation/calcination loop, Chem. Eng. J. 137 (3) (2008) 561–567.

[23] Gemma Grasa, Ramón Murillo, Mónica Alonso, J. Carlos Abanades, Application of the random pore model to the carbonation cyclic reaction, AIChE J. 55 (5) (2009) 1246–1255.

[24] I. Martínez, G. Grasa, R. Murillo, B. Arias, J.C. Abanades, Kinetics of calcination of partially carbonated particles in a Ca-looping system for CO_2 capture, Energy & Fuels 26 (2) (2012) 1432–1440.

[25] Monica Benitez-Guerrero, Beatriz Sarrion, Antonio Perejon, Pedro E. Sanchez-Jimenez, Luis A. Perez-Maqueda, Jose Manuel Valverde, Large-scale high-temperature solar energy storage using natural minerals, Sol. Energy Mater. Sol. Cells 168 (2017) 14–21.

[26] G. Flamant, Theoretical and experimental study of radiant heat transfer in a solar fluidized-bed receiver, AIChE J. 28 (4) (1982) 529–535.

[27] Ricardo Chacartegui Ramírez, José Antonio Becerra Villanueva, José Manuel Valverde Millán, Carlos Ortiz Dominguez, Alessandro Alovisio, Integrated Calcination-Carbonation System and Closed-Loop CO_2 Cycle for Thermochemical Energy Storage and Electrical Energy Generation, WO2017001710A1, 2017, URL: https://patents.google.com/patent/WO2017001710A1/en.

[28] Maurizio Spinelli, Isabel Martínez, Matteo C. Romano, One-dimensional model of entrained-flow carbonator for CO_2 capture in cement kilns by Calcium looping process, Chem. Eng. Sci. 191 (2018) 100–114.

[29] Jorge Plou, Isabel Martínez, Gemma S. Grasa, Ramón Murillo, Experimental carbonation of CaO in an entrained flow reactor, React. Chem. Eng. 4 (5) (2019) 899–908.

[30] J.M. Valverde, M.A.S. Quintanilla, A. Castellanos, Jamming threshold of dry fine powders, Phys. Rev. Lett. 92 (25) (2004) 258303.

[31] Igino Tomasetta, Diego Barletta, Massimo Poletto, The effect of temperature on flow properties of fine powders, Chem. Eng. Trans. 24 (2011) 655–660.

[32] Janewit Phromprasit, Jonathan Powell, Suttichai Assabumrungrat, Metals (Mg, Sr and Al) modified CaO based sorbent for CO_2 sorption/desorption stability in fixed bed reactor for high temperature application, Chem. Eng. J. 284 (2016) 1212–1223.

[33] Hong Lu, Ataullah Khan, Sotiris E. Pratsinis, Panagiotis G. Smirniotis, Flame-made durable doped-CaO nanosorbents for CO_2 capture, Energy & Fuels 23 (2) (2009) 1093–1100.

[34] P. Keith Watson, Jose Manuel Valverde, Antonio Castellanos, The tensile strength and free volume of cohesive powders compressed by gas flow, Powder Technol. 115 (1) (2001) 45–50, http://dx.doi.org/10.1016/S0032-5910(00)00275-8.

[35] Michelle Ramlakhan, Chang Yu Wu, Satoru Watano, Rajesh N. Dave, Robert Pfeffer, Dry particle coating using magnetically assisted impaction coating: modification of surface properties and optimization of system and operating parameters, Powder Technol. 112 (1) (2000) 137–148, http://dx.doi.org/10.1016/S0032-5910(99)00314-9.

[36] Jun Yang, Ales Sliva, Amit Banerjee, Rajesh N. Dave, Robert Pfeffer, Dry particle coating for improving the flowability of cohesive powders, Powder Technol. 158 (1–3) (2005) 21–33.

[37] M.A.S. Quintanilla, J.M. Valverde, A. Castellanos, Adhesion force between fine particles with controlled surface properties, AIChE J. 52 (5) (2006) 1715–1728.

[38] Yuhua Chen, Jun Yang, Rajesh N. Dave, Robert Pfeffer, Fluidization of coated group C powders, AIChE J. 54 (1) (2008) 104–121.

[39] José Manuel Valverde, Antonio Ramos, Antonio Castellanos, P. Keith Watson, The tensile strength of cohesive powders and its relationship to consolidation, free volume and cohesivity, Powder Technol. 97 (3) (1998) 237–245.

[40] Matthew P. Mullarney, Lauren E. Beach, Rajesh N. Davé, Beth A. Langdon, Mark Polizzi, Daniel O. Blackwood, Applying dry powder coatings to pharmaceutical powders using a comil for improving powder flow and bulk density, Powder Technol. 212 (3) (2011) 397–402.

[41] Vikram Karde, Chinmay Ghoroi, Influence of surface modification on wettability and surface energy characteristics of pharmaceutical excipient powders, Int. J. Pharm. 475 (1–2) (2014) 351–363.

[42] M.J. Espin, J.M.P. Ebri, J.M. Valverde, Tensile strength and compressibility of fine $CaCO_3$ powders. Effect of nanosilica addition, Chem. Eng. J. 378 (2019) 122166.

[43] Robert Pfeffer, Rajesh N. Dave, Dongguang Wei, Michelle Ramlakhan, Synthesis of engineered particulates with tailored properties using dry particle coating, Powder Technol. 117 (1–2) (2001) 40–67.

[44] Yuhua Chen, Miguel A.S. Quintanilla, Jun Yang, Jose M. Valverde, Rajesh N. Dave, Pull-off force of coated fine powders under small consolidation, Phys. Rev. E 79 (4) (2009) 041305.

[45] Isaac M. Daniel, Composite Materials: Testing and Design, vol. 787, ASTM International, 1982.

[46] Ramakrishna Gunda, A. Volinsky Alex, Tip-induced calcite single crystal nanowear, MRS Online Proc. Libr. 1049 (1) (2007) 1–6.

[47] Neal S. Gupta, Chitin: Formation and Diagenesis, vol. 34, Springer Science & Business Media, 2010.

[48] Aboutaleb Ghadami Jadval Ghadam, Investigation of mechanical properties prediction of synthesized nylon-66/nano-calcium carbonate composites, J. Part. Sci. Technol. 1 (4) (2015) 241–251.

[49] Seung-Woo Lee, Yong-Jae Kim, Yun-Hee Lee, Hwanuk Guim, Seug Min Han, Behavior and characteristics of amorphous calcium carbonate and calcite using $CaCO_3$ film synthesis, Mater. Des. 112 (2016) 367–373.

[50] Fernando Pacheco-Torgal, Caijun Shi, Angel Palomo, Carbon Dioxide Sequestration in Cementitious Construction Materials, Woodhead Publishing, 2018.

[51] URL: https://www.crystran.co.uk/optical-materials/calcite-caco3.

[52] URL: https://www.surfacenet.de/calcite-217.html.

[53] URL: https://www.hubermaterials.com.

[54] URL: http://www.matweb.com.

[55] Gilson Lomboy, Sriram Sundararajan, Kejin Wang, Shankar Subramaniam, A test method for determining adhesion forces and Hamaker constants of cementitious materials using atomic force microscopy, Cem. Concr. Res. 41 (11) (2011) 1157–1166.

[56] Shri Kant Upadhyay, Seismic Reflection Processing: With Special Reference To Anisotropy, Springer Science & Business Media, 2013.

[57] URL: https://materialsproject.org/materials/mp-3953/.

[58] A.T. Santhanam, Y.P. Gupta, Cleavage surface energy of calcite, Int. J. Rock Mech. Min. Sci. Geomech. Abstracts 5 (3) (1968) 253–259.

[59] Anja Royne, Jan Bisschop, Dag Kristian Dysthe, Experimental investigation of surface energy and subcritical crack growth in calcite, J. Geophys. Res.: Solid Earth 116 (B4) (2011).

[60] URL: http://www.accuratus.com/fused.html.

[61] Lars-Oliver Heim, Jürgen Blum, Markus Preuss, Hans-Jürgen Butt, Adhesion and friction forces between spherical micrometer-sized particles, Phys. Rev. Lett. 83 (16) (1999) 3328.

[62] José Manuel Valverde, Antonio Castellanos, Antonio Ramos, Alberto T. Pérez, Michael A. Morgan, P. Keith Watson, An automated apparatus for measuring the tensile strength and compressibility of fine cohesive powders, Rev. Sci. Instrum. 71 (7) (2000) 2791–2795.

[63] Jörg Schwedes, Review on testers for measuring flow properties of bulk solids, Granul. Matter 5 (1) (2003) 1–43.

[64] Yuhua Chen, Laila Jallo, Miguel A.S. Quintanilla, Rajesh Dave, Characterization of particle and bulk level cohesion reduction of surface modified fine aluminum powders, Colloids Surf. A 361 (1–3) (2010) 66–80.

[65] José Manuel Valverde Millán, Fluidization of Fine Powders: Cohesive Versus Dynamical Aggregation, vol. 18, Springer Science & Business Media, 2012.

[66] U. Zafar, C. Hare, G. Calvert, M. Ghadiri, Rossella Girimonte, Brunello Formisani, M.A.S. Quintanilla, J.M. Valverde, Comparison of cohesive powder flowability measured by schulze shear cell, raining bed method, sevilla powder tester and new ball indentation method, Powder Technol. 286 (2015) 807–816.

[67] Ali Hassanpour, Colin Hare, Massih Pasha, Powder Flow: Theory, Characterisation and Application, Royal Society of Chemistry, 2019.

[68] D. Barletta, M. Poletto, A.C. Santomaso, Bulk powder flow characterisation techniques, in: Powder Flow, Royal Society of Chemistry Cambridge, UK, 2019, pp. 64–146.

[69] Philip Crosbie Carman, Fluid flow through granular beds, Trans. Inst. Chem. Eng. 15 (1937) 150–166.

[70] S.C. Tsinontides, R. Jackson, The mechanics of gas fluidized beds with an interval of stable fluidization, J. Fluid Mech. 255 (1993) 237–274.

[71] Jose Manuel Valverde, Antonio Castellanos, P. Keith Watson, The effect of particle size on interparticle adhesive forces for small loads, Powder Technol. 118 (3) (2001) 236–241.

[72] A. Castellanos, J.M. Valverde, M.A.S. Quintanilla, The sevilla powder tester: a tool for characterizing the physical properties of fine cohesive powders at very small consolidations, KONA Powder Part. J. 22 (2004) 66–81.

[73] Jörg Schwedes, Consolidation and flow of cohesive bulk solids, Chem. Eng. Sci. 57 (2) (2002) 287–294.

[74] Claus Maarup, Klaus Hjuler, Kim Dam-Johansen, High temperature cement raw meal flowability, Powder Technol. 253 (2014) 686–690.

[75] Jose Manuel Valverde, Antonio Castellanos, Antonio Ramos, P. Keith Watson, Avalanches in fine, cohesive powders, Phys. Rev. E 62 (5) (2000) 6851.

[76] K. Rietema, The Dynamics of Fine Powders, Springer Science & Business Media, 2012.

[77] Fridrun Podczeck, Yasmin Mia, The influence of particle size and shape on the angle of internal friction and the flow factor of unlubricated and lubricated powders, Int. J. Pharm. 144 (2) (1996) 187–194.

[78] M.J. Espin, M.A.S. Quintanilla, J.M. Valverde, Effect of particle size polydispersity on the yield stress of magnetofluidized beds as depending on the magnetic field orientation, Chem. Eng. J. 277 (2015) 269–285.

[79] Daniel Bideau, Alex Hansen, Disorder and Granular Media, vol. 3, North Holland, 1993.

[80] Steven T. Nase, Watson L. Vargas, Adetola A. Abatan, J.J. McCarthy, Discrete characterization tools for cohesive granular material, Powder Technol. 116 (2–3) (2001) 214–223.

[81] Hugo C. Hamaker, The London—van der Waals attraction between spherical particles, Physica 4 (10) (1937) 1058–1072.

[82] Yongqing Xu, Cong Luo, Ying Zheng, Haoran Ding, Qiyao Wang, Qiuwan Shen, Xiaoshan Li, Liqi Zhang, Characteristics and performance of CaO-based high temperature CO_2 sorbents derived from a sol–gel process with different supports, RSC Adv. 6 (83) (2016) 79285–79296.

[83] Daizo Kunii, Octave Levenspiel, Fluidization Engineering, Butterworth-Heinemann, 1991.

[84] Sinisa Dj Mesarovic, Norman A. Fleck, Spherical indentation of elastic–plastic solids, Proc. R. Soc. Lond. Ser. A Math. Phys. Eng. Sci. 455 (1987) (1999) 2707–2728.

[85] Sinisa Dj Mesarovic, Norman A. Fleck, Frictionless indentation of dissimilar elastic–plastic spheres, Int. J. Solids Struct. 37 (46–47) (2000) 7071–7091.

[86] Sinisa Dj Mesarovic, K.L. Johnson, Adhesive contact of elastic–plastic spheres, J. Mech. Phys. Solids 48 (10) (2000) 2009–2033.

[87] James Q. Feng, Adhesive contact of elastically deformable spheres: a computational study of pull-off force and contact radius, J. Colloid Interface Sci. 238 (2) (2001) 318–323.

[88] Lior Kogut, Izhak Etsion, Adhesion in elastic–plastic spherical microcontact, J. Colloid Interface Sci. 261 (2) (2003) 372–378.

[89] D. Tabor, Surface forces and surface interactions, J. Colloid Interface Sci. 58 (1) (1977) 2–13, http://dx.doi.org/10.1016/0021-9797(77)90366-6.

[90] Boris V. Derjaguin, Vladimir M. Muller, Yu P. Toporov, Effect of contact deformations on the adhesion of particles, J. Colloid Interface Sci. 53 (2) (1975) 314–326.

[91] D. Maugis, H.M. Pollock, Surface forces, deformation and adherence at metal microcontacts, Acta Metall. 32 (9) (1984) 1323–1334.

[92] K.L. Johnson, Contact Mechanics, vol. 95, Cambridge, 1985, p. 365,

[93] M. Barquins, D. Maugis, Adhesive contact of axisymmetric punches on an elastic half-space: the modified hertz-huber's stress tensor for contacting spheres, J. Mech. Theor. Appl. 1 (1982) 331–357.

[94] J.A. Greenwood, K.L. Johnson, An alternative to the Maugis model of adhesion between elastic spheres, J. Phys. D: Appl. Phys. 31 (22) (1998) 3279.

[95] Leopoldo Massimilla, Giorgio Donsì, Cohesive forces between particles of fluid-bed catalysts, Powder Technol. 15 (2) (1976) 253–260.

[96] E.R. Beach, G.W. Tormoen, J. Drelich, R. Han, Pull-off force measurements between rough surfaces by atomic force microscopy, J. Colloid Interface Sci. 247 (1) (2002) 84–99.

[97] S.K. Roy Chowdhury, N.E.W. Hartley, H.M. Pollock, M.A. Wilkins, Adhesion energies at a metal interface: the effects of surface treatments and ion implantation, J. Phys. D: Appl. Phys. 13 (9) (1980) 1761.

[98] H. Rumpf, Grundlagen und methoden des granulierens, Chem. Ing. Tech. 30 (3) (1958) 144–158, http://dx.doi.org/10.1002/cite.330300307.

[99] M. Nakagaki, H. Sunada, Theoretical studies on structures of the sedimentation bed of spherical particles, Yakugaku Zasshi: J. Pharm. Soc. Japan 88 (6) (1968) 651–655.

[100] M. Seipenbusch, S. Rothenbacher, M. Kirchhoff, H.-J. Schmid, G. Kasper, A.P. Weber, Interparticle forces in silica nanoparticle agglomerates, J. Nanopart. Res. 12 (6) (2010) 2037–2044.

[101] J. Ruud van Ommen, Jose Manuel Valverde, Robert Pfeffer, Fluidization of nanopowders: a review, J. Nanopart. Res. 14 (3) (2012) 1–29.

[102] Roger G. Horn, Douglas T. Smith, Contact electrification and adhesion between dissimilar materials, Science 256 (5055) (1992) 362–364.

[103] Weiqiang Zhang, Qiang Sun, Shuyun Zhu, Bo Wang, Experimental study on mechanical and porous characteristics of limestone affected by high temperature, Appl. Therm. Eng. 110 (2017) 356–362.

[104] M.D. Michel, F.C. Serbena, C.M. Lepienski, Effect of temperature on hardness and indentation cracking of fused silica, J. Non-Cryst. Solids 352 (32–35) (2006) 3550–3555.

[105] Jacob N. Israelachvili, Intermolecular and Surface Forces, Academic Press, 2015.

[106] Muhammad Tufail, Khan Shahzada, Bora Gencturk, Jianqiang Wei, Effect of elevated temperature on mechanical properties of limestone, quartzite and granite concrete, Int. J. Concr. Struct. Mater. 11 (1) (2017) 17–28.

[107] Jian Yang, Li-Yun Fu, Weiqiang Zhang, Zhiwei Wang, Mechanical property and thermal damage factor of limestone at high temperature, Int. J. Rock Mech. Min. Sci. 117 (2019) 11–19.

[108] Euan J. Boyd, Li Li, Robert Blue, Deepak Uttamchandani, Measurement of the temperature coefficient of Young's modulus of single crystal silicon and 3C silicon carbide below 273 K using micro-cantilevers, Sensors Actuators A 198 (2013) 75–80.